Journal of Photochemistry & Photobiology, A: Chemistry 476 (2026) 117068

Contents lists available at ScienceDirect

Journal of Photochemistry & Photobiology, A: Chemistry

journal homepage: www.elsevier.com/locate/jphotochem

Serendipitous discovery of nitrogen bridgehead fused pyridines: photophysical properties and live-cell imaging potential

Hana Kokot [a], Aljoša Bolje [b], Jakob Kljun [c], Andraž Bevk [b], Natalija Trunkelj [b], Lucija Peterlin Mašič [b], Janez Mravljak [b,*], Stane Pajk [b,*]

[a] Jožef Stefan Institute, Jamova cesta 39, 1000 Ljubljana, Slovenia
[b] University of Ljubljana, Faculty of Pharmacy, Aškerčeva cesta 7, 1000 Ljubljana, Slovenia
[c] University of Ljubljana, Faculty of Chemistry and Chemical Technology, Večna pot 113, 1000 Ljubljana, Slovenia

ARTICLE INFO

Keywords:
Nitrogen bridgehead fused pyridine
Fluorescence
pH sensitive probes
Live-cell imaging
Fluorescence lifetime imaging

ABSTRACT

A novel synthetic route to fluorescent nitrogen bridgehead fused pyridines (NBFPs) was discovered serendipitously during attempts to synthesize a thiazole derivative via a Hantzsch-type thiazole reaction from 2-cyanoethanethioamide and chloroacetone. A mechanism was proposed to rationalize the formation of NBFPs, which guided the subsequent expansion of the reaction scope and optimization of reaction conditions. The scope of the reaction was extended to include arylacetonitriles and esters of 2-(heteroaryl)acetic acids bearing an ortho-positioned pyridine-type nitrogen as a starting material. The structures of selected compounds were confirmed by single-crystal X-ray diffraction. All synthesized NBFPs exhibited pH-sensitive fluorescence and Stokes shifts exceeding 100 nm in several cases. Two compounds, methylthiazole derivative **1** and quinoline derivative **8**, displayed pH-dependent emission suitable for lysosomal labelling. However, live-cell microscopy revealed limited colocalization with lysosomal probe Lysotracker Red, suggesting that these probes may localize to other acidic environments as well. Both compounds showed pronounced spectral responsiveness and fluorescence lifetime variations, indicating potential for use as environment-sensitive intracellular sensors. The methyl thiazole derivative **1** exhibited particularly favourable properties, including high photostability, low background fluorescence, minimal cytotoxicity and polarity sensitivity. These findings position NBFPs as a promising class of fluorophores for live-cell imaging and intracellular sensing applications, and warrant further investigation into their structure–function relationships and environmental responsiveness.

1. Introduction

The phenomenon of fluorescence underpins numerous techniques in medicine, biology, physics, and chemistry. These techniques predominantly rely on extrinsic fluorescent labels or probes, which are essential for imaging, diagnostics, and analytical assays [1,2]. With the rapid advancement of fluorescence-based methods, the demand for suitable fluorescent probes has grown substantially. However, the limited availability of such probes often constrains the full potential of these techniques. In the past decade, significant progress has been made in understanding the principles governing the design of fluorescent probes and in fine-tuning their photophysical properties [3,4]. Nevertheless, unlike drug discovery, where *in silico* methods have become integral, the design of new fluorescent scaffolds has yet to fully benefit from computational approaches. This is particularly evident in the development of fluorophores with large Stokes shifts or those emitting in the far-red region [3]. Consequently, the discovery of new fluorophores still relies heavily on empirical approaches and serendipitous findings [5].

During an attempt to synthesize thiazole **A**, a reaction mixture comprising 1-chloroacetone, 2-cyanoethanethioamide, and solvent dimethylformamide (DMF) was stirred for three weeks at room temperature (Scheme 1). Thin-layer chromatography (TLC) analysis of the reaction mixture revealed that the primary product was indeed thiazole **A**. However, a significant by-product exhibiting distinctive green fluorescence under UV light was also observed. Upon isolation and characterization, the structure of this fluorescent by-product was identified as compound **1** (Scheme 1), which is structurally nitrogen bridgehead fused pyridine (NBFP).

Recently, significant attention has been focused on the NBFP

* Corresponding authors.
E-mail addresses: janez.mravljak@ffa.uni-lj.si (J. Mravljak), stane.pajk@ffa.uni-lj.si (S. Pajk).

https://doi.org/10.1016/j.jphotochem.2026.117068
Received 10 October 2025; Received in revised form 22 December 2025; Accepted 25 January 2026
Available online 26 January 2026

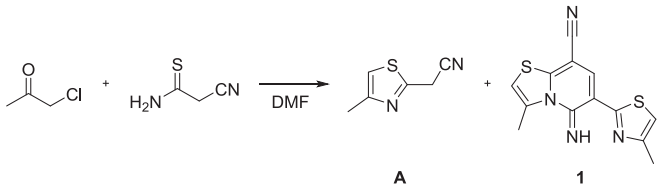

Scheme 1. Synthesis of 2-(4-methyl-1,3-thiazol-2-yl)acetonitrile (**A**) and NBFP by-product **1**.

derivative **IMQU-8**, also known as **IPQC** (Scheme 2) [6,7]. This compound has demonstrated versatile applications as a pH probe, lysosome label, DNA label, and sensor for Pd^{2+} [6–8]. Besides **IMQU-8**, other derivatives, such as those derived from benzothiazole and benzimidazole, have also been documented [9]. Various synthetic pathways to NBFP have been published recently, all of which start from arylacetonitriles with a pyridine-type nitrogen at the ortho position of the aromatic ring.

Gong et al. reported a straightforward synthesis of **IPQC** (**IMQU-8**) from 2-pyridylacetonitrile and DMF in the presence of a strong base, NaHMDS (Scheme 2A), achieving a good yield [8]. However, the applicability of this reaction to other arylacetonitriles remains unknown. Yang et al. described a synthesis involving 2-pyridylacetonitrile and (*Z*)-3-ethoxy-2-arylacrylonitrile in the presence of sodium ethoxide as a base (Scheme 2B) [7]. Although this method requires several steps to prepare suitable (*Z*)-3-ethoxy-2-arylacrylonitriles, it allows the introduction of various aryl groups onto the cyanopyridine core, facilitating the fine-tuning of the products' physical and photophysical properties.

A more diverse approach to synthesizing cyanopyridines was presented by Milokhov et al. [9]. In their method, 2-hetaryl-2-(tetrahydro-2-furanyliden)acetonitriles are first prepared in a two-step reaction from hetarylacetonitriles and then reacted with arylacetonitriles in the presence of a strong base, NaH (Scheme 2C). This strategy offers a versatile pathway for creating a wide range of cyanopyridine derivatives.

In this paper, we present the serendipitous discovery of a novel synthetic pathway to NBFP. Building upon the initial reaction conditions, we further developed and optimized the reaction. The scope of the reaction was explored using various hetarylacetonitriles as starting materials. Additionally, we demonstrate that esters of 2-(heteroaryl) acetic acid can also react under these reaction conditions to form ester analogs of NBFP. The structures of several products were confirmed by single crystal X-ray diffraction. Furthermore, we recorded the absorption and emission spectra of the synthesized compounds in buffer solutions at different pH, noting that the emission of all synthesized NBFP

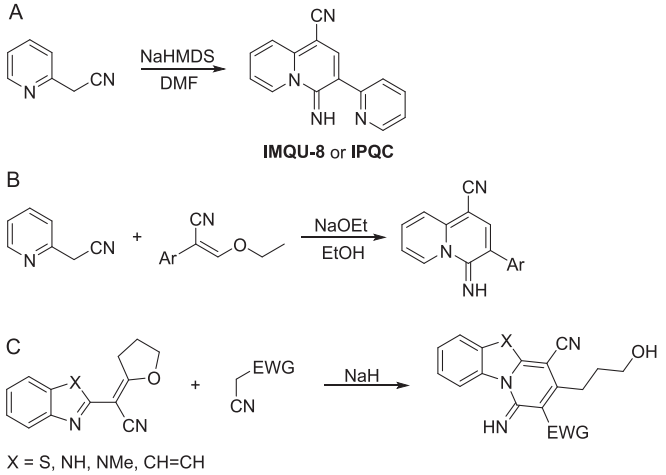

Scheme 2. Selected recently published synthetic pathways to NBFPs.

was pH-sensitive. Based on their photophysical properties, we selected thiazole and quinoline derivatives for further investigation of their bioimaging capabilities. This study not only broadens the scope of NBFPs synthesis but also highlights their potential applications in bioimaging.

2. Experimental

2.1. Materials and methods

Chemicals from Sigma-Aldrich, Apollo Scientific, TCI, and Acros Organics were used as received without further purification. All reactions were performed under an argon atmosphere, unless otherwise noted. Analytical thin-layer chromatography (TLC) was conducted on Merck silica gel 60 F_{254} plates (0.25 mm) and visualized under ultraviolet light. ^{1}H and ^{13}C nuclear magnetic resonance (NMR) spectra were recorded on a Bruker AVANCE III 400 MHz NMR spectrometer, using $CDCl_3$, TFA-*d*, pyridine-d_5, DMSO-d_6 or methanol-d_4 as solvents, with chemical shifts referenced to tetramethylsilane (TMS) or the residual solvent peaks. Mass spectra were obtained using a Thermo Scientific Q Exactive Plus Hybrid Quadrupole-Orbitrap mass spectrometer. Fluorescence and absorption spectra were measured using a Horiba Duetta fluorescence spectrophotometer and an Agilent Cary 60 UV–Vis spectrophotometer, respectively. Further details regarding solvents, concentrations, and solution pH used for absorption, excitation, and emission measurements are provided in the Supplementary data.

2.2. Synthesis and characterization

2.2.1. General procedure A

Arylacetonitrile (3.46 mmol, 1 M equiv) was dissolved in DMF 2.7 (mL). A 4 M solution of hydrochloric acid in dioxane (3.46 mL, 13.8 mmol, 4 M equiv) was added dropwise to the reaction mixture, which was then stirred at 60 °C for 2 days. After completion, the reaction mixture was cooled to room temperature, and the resulting precipitate was filtered off and washed with 15 mL of diethyl ether.

2.2.2. General procedure B

2-Cyanoethanethioamide (1.80 g, 8.37 mmol, 1 M equiv) and α-halo ketone (8.37 mmol, 1 M equiv) were dissolved in 6.5 mL of DMF. The reaction mixture was stirred at room temperature overnight. Subsequently, a 4 M solution of hydrochloric acid in dioxane was added to the reaction mixture, which was then stirred at 60 °C for 3 days. The resulting precipitate was filtered off and washed with diethyl ether.

Regardless of the general procedure used, compounds **1**–**8** were isolated as salts corresponding to the acids used as catalysts in the reactions. For analytical purposes, primarily to improve solubility in deuterated solvents, compounds **2**, **3**, **5** and **7** were converted to their neutral forms by washing their dichloromethane suspensions with a saturated $NaHCO_3$ solution.

2.2.2.1. 5-Imino-3-methyl-6-(4-methylthiazol-2-yl)-5H-thiazolo[3,2-a] pyridine-8-carbonitrile (1). Compound **1** was prepared and isolated as described under General procedure A, 2-(4-methyl-1,3-thiazol-2-yl) acetonitrile was used as starting material, to give the desired product (83%) as a light orange solid. NMR spectra were recorded for compound **1** as its HCl salt. ^{1}H NMR (400 MHz, Pyr-d_5) δ 7.78 (s, 1H), 7.03 (q, J = 1.0 Hz, 1H), 6.87 (q, J = 1.2 Hz, 1H), 2.92 (d, J = 1.2 Hz, 3H), 2.40 (d, J = 1.0 Hz, 3H). ^{13}C NMR (101 MHz, Pyr-d_5) δ 165.71, 160.41, 155.23, 153.36, 143.08, 133.09, 118.33, 113.69, 113.36, 108.96, 78.89, 20.65, 17.58. HRMS (ESI): *m/z* calcd for $C_{13}H_{10}N_4S_2$ $[M + H]^+$ 287.04196; found 287.04096.

2.2.2.2. 5-Imino-3-phenyl-6-(4-phenylthiazol-2-yl)-5H-thiazolo[3,2-a] pyridine-8-carbonitrile (2). Compound **2** was prepared and isolated as

described under General procedure A, 2-(4-phenylthiazol-2-yl)acetonitrile was used as starting material, to give the desired product (36%) as a light yellow solid. NMR spectra were recorded for compound **2** in its free base form. ^{1}H NMR (400 MHz, TFA-*d*) δ 9.25 (s, 1H), 8.42 (s, 1H), 8.39–8.31 (m, 2H), 8.28–8.19 (m, 6H), 7.98–7.91 (m, 3H). ^{13}C NMR (101 MHz, TFA-*d*) δ 160.11, 158.71, 153.52, 144.65, 141.33, 135.79, 133.74, 132.60, 132.34, 131.52, 128.57, 123.00, 117.84, 114.34, 112.09, 95.45. HRMS (ESI): *m/z* calcd for $C_{23}H_{15}N_4S_2$ $[M + H]^+$ 411.07326; found 411.07257.

2.2.2.3. 3-(4-Hydroxyphenyl)-6-(4-(4-hydroxyphenyl)thiazol-2-yl)-5-imino-5H-thiazolo[3,2-a]pyridine-8-carbonitrile (3). Compound **3** was prepared and isolated as described under General procedure B, 2-bromo-1-(4-hydroxyphenyl)ethan-1-one was used as starting material, to give the desired product (61%) as a yellow solid. NMR spectra were recorded for compound **3** as its HCl salt. ^{1}H NMR (400 MHz, TFA-*d*) δ 9.42 (s, 1H), 8.61 (s, 1H), 8.56 (s, 1H), 8.50–8.35 (m, 4H), 8.03–7.97 (m, 2H), 7.83–7.77 (m, 2H). ^{1}H NMR (400 MHz, DMSO-d_6) δ 8.66 (s, 1H), 7.66–7.52 (m, 4H), 6.98 (s, 2H), 6.64–6.50 (m, 4H). ^{13}C NMR (101 MHz, DMSO-d_6) δ 167.35, 166.28, 155.56, 138.54, 127.15, 120.86, 119.58, 117.11, 100.54, 74.27. Potassium butoxide (5% *w*/w) was added to DMSO-d_6 prior to recording the ^{1}H and ^{13}C NMR spectra. HRMS (ESI): *m/z* calcd for $C_{23}H_{15}O_2N_4S_2$ $[M + H]^+$ 443.06309; found 443.06268.

2.2.2.4. 3-(tert-Butyl)-6-(4-(tert-butyl)thiazol-2-yl)-5-imino-5H-thiazolo[3,2-a]pyridine-8-carbonitrile (4). Compound **4** was prepared as described under General procedure B, 1-chloro-3,3-dimethylbutan-2-one was used as starting material, to give the desired product (54%) as a pink solid. NMR spectra were recorded for compound **4** in its free base form. ^{1}H NMR (400 MHz, DMSO-d_6) δ 8.15–7.81 (m, 1H), 6.92 (s, 2H), 1.30 (s, 18H). ^{1}H NMR (400 MHz, TFA-*d*) δ 8.52 (s, 1H), 7.52 (s, 2H), 1.95 (s, 18H). ^{13}C NMR (101 MHz, TFA-*d*) δ 173.41, 159.64, 146.78, 116.11, 111.31, 80.19, 36.45, 30.11. HRMS (ESI): *m/z* calcd for $C_{19}H_{23}N_4S_2$ $[M + H]^+$ 371.13586; found 371.13522.

2.2.2.5. 2-(Benzo[d]thiazol-2-yl)-1-imino-1H-benzo[4,5]thiazolo[3,2-a]pyridine-4-carbonitrile (5). Compound **5** was prepared as described under General procedure A, 2-(benzo[*d*]thiazol-2-yl)acetonitrile was used as starting material, to give the desired product (64%) as a yellow solid. NMR spectra in DMSO-d_6 were recorded for compound **5** as its HCl salt. Potassium butoxide (5% *w*/w) was added to DMSO-d_6 prior to recording the ^{1}H and ^{13}C NMR spectra. ^{1}H NMR (400 MHz, DMSO-d_6) δ 8.46 (s, 1H), 7.90–7.86 (m, 2H), 7.73–7.68 (m, 2H), 7.36 (ddd, J = 8.3, 7.3, 1.3 Hz, 2H), 7.22–7.15 (m, 2H). ^{13}C NMR (101 MHz, DMSO-d_6) δ 167.99, 154.36, 140.08, 132.77, 126.00, 122.53, 121.41, 119.95, 119.26, 76.89. NMR spectrum in TFA-*d* was recorded for compound **5** in its free base form. ^{13}C NMR (101 MHz, TFA-*d*) δ 164.07, 160.03, 155.77, 153.41, 142.77, 138.69, 135.66, 133.76, 131.90, 130.78, 130.66, 129.66, 127.32, 125.35, 124.05, 120.21, 114.41, 114.16, 95.49. HRMS (ESI): *m/z* calcd for $C_{19}H_{11}N_4S_2$ $[M + H]^+$ 359.04196; found 359.04129.

2.2.2.6. 2-(benzo[d]thiazol-2-yl)-1-imino-1H-benzo[4,5]thiazolo[3,2-a]pyridine-4-carbonitrile-3-d (5-d_1). Compound **5-d_1** was prepared and isolated as described under General procedure A, 2-(benzo[*d*]thiazol-2-yl)acetonitrile and *N*,*N*-dimethylformamide-d_7 were used as starting material, to give the desired product (83%) as a yellow solid. NMR spectrum in DMSO-d_6 was recorded for compound **5-d_1** as its HCl salt. Potassium butoxide (5% *w*/w) was added to DMSO-d_6 prior to recording the ^{1}H NMR spectrum. ^{1}H NMR (400 MHz, DMSO-d_6) δ (ppm) 7.90–7.88 (m, 2H, H—Ar), 7.72–7.70 (m, 2H, H—Ar), 7.39–7.35 (m, 2H, H—Ar), 7.21–7.17 (m, 2H, H—Ar). HRMS (ESI): *m/z* calcd for $C_{19}H_{10}DN_4S_2$ $[M + H]^+$ 360.04824; found 360.04748.

2.2.2.7. 2-(1H-Benzo[d]imidazol-2-yl)-1-imino-1,5-dihydrobenzo[4,5]imidazo[1,2-a]pyridine-4-carbonitrile (6). Compound **6** was prepared as described under General procedure A, 2-(1*H*-benzo[*d*]imidazol-2-yl)acetonitrile was used as starting material, to give the desired product (79%) as an off-white solid. Alternatively, methanesulfonic acid was used instead of hydrochloric acid to give the desired product (41%) as off-white solid. NMR spectrum was recorded for compound **6** as its mesylate salt. ^{1}H NMR (400 MHz, DMSO-d_6) δ 8.83 (s, 1H), 8.68–8.60 (m, 1H), 7.90–7.84 (m, 1H), 7.73–7.60 (m, 3H), 7.57–7.48 (m, 1H), 7.33–7.21 (m, 2H), 2.41 (s, 3H). NMR spectra were recorded for compound **6** as its HCl salt. ^{1}H NMR (400 MHz, TFA-*d*) δ 9.60 (s, 1H), 9.39–9.33 (m, 1H), 8.95–8.86 (m, 2H), 8.82–8.72 (m, 3H), 8.71–8.64 (m, 2H). ^{13}C NMR (101 MHz, TFA-*d*) δ 153.31, 147.47, 147.33, 143.75, 134.21, 134.10, 133.68, 131.51, 129.76, 129.09, 117.58, 117.11, 116.69, 113.83, 98.43, 84.81. HRMS (ESI): *m/z* calcd for $C_{19}H_{13}N_6$ $[M + H]^+$ 325.11961; found 325.11902.

2.2.2.8. 4-Imino-3-(pyridin-2-yl)-4H-quinolizine-1-carbonitrile (7). Compound **7** was prepared as described under general procedure A, 2-(pyridin-2-yl)acetonitrile was used as starting material and the reaction mixture was heated at 80 °C for 4 days, to give the desired product (84%) as a pale orange solid. Alternatively, hydrobromic acid was used instead of hydrochloric acid to give the desired product (33%) as a pale orange solid. NMR spectra were recorded for compound **7** in its free base form. ^{1}H NMR (400 MHz, $CDCl_3$) δ 10.36 (bs, 1H), 9.72–9.59 (m, 1H), 8.68 (ddd, J = 5.0, 1.8, 0.9 Hz, 1H), 7.83–7.73 (m, 2H), 7.67 (s, 1H), 7.64–7.57 (m, 2H), 7.26 (ddd, J = 7.5, 5.0, 1.1 Hz, 1H), 7.06 (ddd, J = 7.4, 6.7, 1.5 Hz, 1H). ^{13}C NMR (101 MHz, $CDCl_3$) δ 156.10, 154.35, 148.49, 146.45, 137.17, 134.93, 133.35, 130.90, 122.78, 122.02, 121.71, 118.72, 115.82, 115.48, 79.52. HRMS (ESI): *m/z* calcd for $C_{15}H_{11}N_4$ $[M + H]^+$ 247.09782; found 247.09718.

2.2.2.9. 4-Imino-3-(quinolin-2-yl)-4H-pyrido[1,2-b]isoquinoline-1-carbonitrile (8). Compound **8** was prepared as described under general procedure A, 2-(quinolin-2-yl)acetonitrile was used as starting material, to give the desired product (90%) as a dark red solid. NMR spectra were recorded for compound **8** as its HCl salt. ^{1}H NMR (400 MHz, TFA-*d*) δ 9.77 (s, 1H), 9.06–8.97 (m, 2H), 8.95–8.85 (m, 2H), 8.49–8.34 (m, 6H), 8.24–8.16 (m, 2H). ^{13}C NMR (101 MHz, TFA-*d*) δ 154.32, 147.32, 146.58, 140.51, 137.47, 131.31, 131.24, 128.15, 121.49, 121.33, 84.41, 69.19. HRMS (ESI): *m/z* calcd for $C_{23}H_{15}N_4$ $[M + H]^+$ 347.12912; found 347.12860.

2.2.2.10. Ethyl 2-(benzo[d]oxazol-2-yl)-1-oxo-1H-benzo[4,5]oxazolo[3,2-a]pyridine-4-carboxylate (9). Compound **9** was prepared as described under general procedure A, ethyl 2-(benzo[*d*]oxazol-2-yl)acetate was used as starting material, to give the desired product (35%) as a white solid. ^{1}H NMR (400 MHz, TFA-*d*) δ 9.48 (s, 1H), 8.58–8.50 (m, 1H), 7.94–7.87 (m, 1H), 7.86–7.65 (m, 6H), 4.59 (q, J = 7.2 Hz, 2H), 1.48 (t, J = 7.2 Hz, 3H). ^{13}C NMR (101 MHz, TFA-*d*) δ 165.78, 162.72, 160.23, 159.71, 150.60, 150.08, 147.96, 132.67, 131.99, 131.42, 130.45, 129.84, 127.50, 119.41, 117.67, 114.51, 114.45, 102.07, 100.62, 66.90, 14.77. HRMS (ESI): *m/z* calcd for $C_{21}H_{15}N_2O_5$ $[M + H]^+$ 375.09755; found 375.09680.

2.2.2.11. Ethyl 2-(benzo[d]thiazol-2-yl)-1-oxo-1H-benzo[4,5]thiazolo[3,2-a]pyridine-4-carboxylate (10). Compound **10** was prepared as described under general procedure A, ethyl 2-(benzo[*d*]thiazol-2-yl)acetate was used as starting material, to give the desired product (41%) as a yellow solid. ^{1}H NMR (400 MHz, TFA-*d*) δ 10.10–10.02 (m, 1H), 9.86 (s, 1H), 8.90–8.82 (m, 1H), 8.81–8.74 (m, 1H), 8.73–8.67 (m, 1H), 8.57–8.38 (m, 4H), 5.33 (q, J = 7.1 Hz, 2H), 2.24 (t, J = 7.2 Hz, 3H). ^{13}C NMR (101 MHz, TFA-*d*) δ 171.43, 167.63, 164.42, 163.99, 162.86, 162.49, 142.22, 141.73, 139.90, 133.01, 131.87, 131.51, 131.46, 130.68, 125.13, 124.78, 123.16, 119.70, 109.24, 108.37, 67.27, 15.02. HRMS (ESI): *m/z* calcd for $C_{21}H_{15}O_3N_2S_2$ $[M + H]^+$ 407.05186; found 407.05175.

2.2.3. Single crystal X-ray structural analysis

Single crystal X-ray diffraction data was collected at 150 K on a SuperNova diffractometer with Atlas detector using CrysAlis software with monochromated Mo Kα (0.71073 Å) [Oxford Diffraction Ltd., CrysAlis PRO, Yarnton, Oxfordshire, England, 2011]. The initial structural models were solved with direct methods implemented in SHELXT using the *Olex*2 graphical user interface [10]. A full-matrix least-squares refinement on F^2 magnitudes with anisotropic displacement parameters for all non-hydrogen atoms using *Olex*2 or *SHELXL*-2018/3 was performed [10]. All non-hydrogen atoms were refined anisotropically, while hydrogen atoms were placed at calculated positions and treated as riding on their parent atoms. Details on the crystal data, data acquisition and refinement are presented in Table S2. Mercury [11] was used for preparation of the figures. CCDC deposition numbers 2,374,858–2,374,860 contain the supplementary crystallographic data for this paper.

2.2.4. pKa determination

To determine pK_a values of compounds **1** and **8**, their pH-dependant fluorescence intensity was fitted, as derived in [12] (eq. 33). Based on the diprotic chemical structures of the compounds, we expect two pK_a, and therefore used a two-component fit:

$$I = bc_t \frac{\varepsilon^{\lambda}_{H_2A^z} + \sum_{i=1}^{2} \varepsilon^{\lambda}_{H_{2-i}A^{z-i}} 10^{i\,pH - \sum_{j=1}^{i} pK'_{aj}}}{1 + \sum_{i=1}^{2} 10^{i\,pH - \sum_{j=1}^{i} pK'_{aj}}}$$

where b denotes the path length of light, c_t the total concentration of the compound, and ε^{λ} the molar absorptivity at the measurement wavelength λ. Subscript indexes correspond to the species [HHA], [HA] and [A]. For fitting we simplified the expression to

$$I = \alpha \frac{\beta + \gamma_1 10^{pH - pK'_{a1}} + \gamma_2 10^{2pH - pK'_{a1} - pK'_{a2}}}{1 + 10^{pH - pK'_{a1}} + 10^{2pH - pK'_{a1} - pK'_{a2}}}$$

The measurements were fitted in Python using the function *scipy.optimize.curve_fit* with the constraint of non-negative fit parameters.

2.3. Live-cell imaging and fluorescence lifetime measurements

For fluorescence imaging, the cell line of murine type II pneumocytes LA-4 (ATCC Ccl-196) was cultured in a controlled environment (5% CO_2, 37 °C) according to ATCC guidelines. After growing in T25 flasks (TPP) they were seeded into 18-well glass bottom chambers (Cellvis) for imaging. Cells were cultured and imaged in full cell culture media, consisting of F-12 K medium (Gibco), 15% FBS (Gibco), 1% NEAA (Gibco), 1% GlutaMAX (Gibco), and 1% P/S (Gibco). Just prior to imaging, the dried dyes were resuspended in DMSO (20 mM) and diluted to a working concentration of 20 μM in complete cell medium. For localization experiments, the cells were also labelled with the commercial LysoTracker Red dye (Invitrogen, 50 nM, 2 h).

Imaging was performed on a custom-built confocal/STED laser-scanning microscope (Abberior Instruments) with a 60× water immersion objective (NA 1.2) and a stage-top incubator (5% CO_2, 37 °C). Fluorescence was excited using a pulsed laser (405 nm, 488 nm, 518 nm, 561 nm, or 640 nm) and detected using three APDs (filter sets 500–548 nm, 581–627 nm, and 651–720 nm). For STED imaging, a 775 nm STED laser was also used (2D STED, power 380 μW in the sample plane). Fluorescence lifetime imaging (FLIM) was performed with the aforedescribed APDs using a TCSPC card (Becker & Hickl) integrated in the microscope. For comparing the photostability of the probes, a 10 × 10 μm large field of view was imaged consequently 30 times at three positions on the sample; the unbound probe was left in the sample during imaging. The intensity of the inner 5 × 5 μm field of view was summed up for intensities above the noise threshold (5 counts) and plotted versus time. The intensity was in the linear region of the detector to prevent artefacts from detector saturation.

The images were analyzed using Imspector 16.3 (Abberior Instruments), and the fluorescence lifetimes were analyzed with SPCImage software 7.3 (Becker & Hickl) using binning 2, threshold value of 100, and an incomplete multi-exponential fit due to the short repetition time of the excitation lasers (12.5 ns). To characterise the lifetime of compounds in various solvents, the 512 × 512 images were binned into 21 × 21 large bins (binning 10), and the fluorescence decay equation was fitted for each bin separately to determine the mean and standard deviation of the lifetime distribution. In several cases, the signal was so low that the entire image was pooled together for fitting, in which case the error of the lifetime is not given.

The photostability was quantified by fitting an exponential curve to the normalised fluorescence intensity in the sequence of images:

$$I_n/I_1 = a + (1-a)e^{-b(n-1)}$$

where a corresponds to the intensity baseline, b to the photobleaching rate, and n to the consecutive image in the sequence (counting starts with 1). As three independent measurements were performed on different regions in the sample, fitting was performed on their mean, and their standard deviation was used as weights. The *NonlinearModelFit* function from Wolfram Mathematica was used for fitting and parameter error determination.

3. Results and discussion

3.1. Chemistry

After isolation and identification of side product **1**, a reaction mechanism was proposed involving the initial formation of methylthiazoleacetonitrile through the condensation of 1-chloroacetone with 2-cyanoethanethioamide, accompanied by the release of hydrogen chloride. The liberated HCl is presumed to activate DMF, initiating the subsequent cyclization that affords the NBFP (Scheme 1). To validate this hypothesis, the reaction was performed using methylthiazoleacetonitrile as the substrate in DMF with four molar equivalents of 4 M HCl in dioxane, which afforded the expected product, thereby supporting the proposed mechanism.

The initial reaction employing 1-chloroacetone and 2-cyanoethanethioamide yielded only 10% of the desired compound, prompting further optimization of the reaction conditions, particularly with respect to the acid catalyst (Table 1). The transformation proceeded exclusively

Table 1
Screening of acid catalysts.

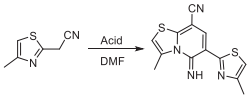

Entry	Acid catalyst (molar equiv)	Yield[a] (%)
1	HCl[b] (1)	48
2	HCl[b] (2)	82
3	HCl[b] (3)	85
4	HCl[b] (4)	83
5	HBr[c] (4)	18
6	H_2SO_4 (4)	72
7	PTSA (4)	28
8	Acetic acid (4)	0
9	CF_3COOH (4)	8
10	H_3PO_4 (4)	0
11	MsOH (4)	73
12	/	0

The screening reaction conditions: 2-(4-methyl-1,3-thiazol-2-yl)acetonitrile 0.35 mmol, 270 μL DMF, 60 °C, 2 days.

[a] Yields were determined by HPLC analysis (see Supp. Data).

[b] 4 M solution in dioxane

[c] 30% solution in acetic acid

in the presence of strong acids. Acetic and phosphoric acid failed to yield the target product, while trifluoroacetic acid produced only small amounts. The highest yield was obtained using three molar equivalents of HCl; however, four molar equivalents were selected for subsequent experiments, as this condition facilitated efficient precipitation of the product in the form of the hydrochloride salt.

We further examined the role of DMF by substituting it with a deuterated DMF. As expected, deuterium was incorporated into the product at position 7 (**5-*d*$_1$**), confirming the role of DMF in the reaction mechanism. Additional insights were obtained through LCMS analysis of selected reaction mixtures used to determine the yield. In some reaction mixtures, an additional peak corresponding to vinylogous aminonitrile 3-(dimethylamino)-2-(4-methylthiazol-2-yl)acrylonitrile was observed (Fig. S2 and S3). This intermediate likely forms through the reaction between methylthiazoleacetonitrile and protonated DMF. In the next step, it reacts with another molecule of methylthiazoleacetonitrile, eliminating dimethylamine and forming the final product through cyclization (Scheme 3).

In the next step, we explored the applicability of the reaction to other arylacetonitriles beyond methylthiazoleacetonitrile. This expansion was undertaken in a chemistry-driven, exploratory manner, primarily guided by the availability of suitable starting materials. Several thiazole derivatives were synthesized using two different approaches. In the first approach, thiazoles were formed by reacting 2-cyanoethanethioamide derivatives with the appropriate α-haloketone in DMF, followed by addition of HCl in dioxane, resulting in compounds **1**–**4** (Fig. 1). Alternatively, we began the reaction directly with various commercially available arylacetonitriles, which led to the synthesis of compounds **1** and **5**–**8**. All of these compounds precipitated out of the reaction mixture, allowing for easy isolation by filtration. Furthermore, we substituted arylacetonitrile with ethyl 2-arylacetate, successfully producing esters **9** and **10**.

In comparison with previously reported synthetic approaches to this class of fluorophores, the method described herein affords the target compounds in a single step and in good yields, with further scope for optimization. Moreover, the reaction procedure is technically straightforward and does not require expensive reagents or catalysts, and can be readily performed on a gram scale. In this respect, it is comparable to the method reported by Gong et al. (Scheme 2A) [8]. Such simplicity is advantageous when the fluorophores are intended for use as standalone probes. A limitation of this approach, however, is the restricted potential for post-synthetic modification, which limits both fine-tuning of photophysical properties and the introduction of functional groups necessary for bioconjugation. Although this limitation could be addressed by introducing a functional group into the arylacetonitrile precursor, this modification would require additional synthetic steps. In contrast, greater flexibility in tuning photophysical properties and incorporating functionalization handles is more readily achieved using the synthetic methodologies reported by Yang et al. (Scheme 2B) [7] or Milokhov et al. (Scheme 2C) [9], albeit at the expense of additional reaction steps.

The structures of the NBFP were further confirmed by determining the crystal structures of three of the products synthesized (Fig. 2). Tables containing the crystallographic data and photographs of the analyzed crystals as well as the bulk crystals of compound **7** are included in the Supplementary data (Tables S2 and S3).

3.2. Photophysical properties

Given the well-documented pH sensitivity of NBFPs, the absorption and emission spectra of compounds **1**–**8** were recorded in Britton-Robinson universal buffer over a pH range of 2–10 to evaluate their photophysical properties (Fig. 3 and S6). With the exception of compound **3**, all compounds exhibited stronger emission at low pH values and little to no emission at higher pH. In contrast, compound **3** displayed the opposite trend, although its overall fluorescence intensity was very weak. A decrease in solubility was observed for all NBFPs at higher pH values, and for some compounds, absorption spectra could not be recorded under these conditions due to precipitation. This behaviour is attributed to protonation of the imine moiety at low pH, which enhances solubility in aqueous media, whereas deprotonation at higher pH decreases solubility. The absorption and emission spectra of esters **9** and **10** were recorded in ethanol (Fig. S5), as their fluorescence is not pH-dependent within the physiological range and both compounds exhibit poor solubility in aqueous solutions.

All synthesized imine derivatives (**1**–**8**) exhibited large Stokes shifts, exceeding 100 nm in most cases (Table 2). However, compounds **3** and **4** showed extremely weak fluorescence across the entire investigated pH range. In the case of compound **3**, this behaviour is likely attributable to the presence of phenolic substituents with strong electron-donating properties, as compound **2**, which lacks these moieties, displayed pronounced emission. The weak fluorescence of compound **4** is less readily explained, particularly given that its methyl-substituted analogue exhibited strong emission. One possible explanation is steric hindrance introduced by the bulkier *tert*-butyl groups. For both compounds **3** and **4**, the emission intensity was insufficient to allow meaningful determination of fluorescence quantum yields. In contrast, the remaining imine derivatives exhibited moderate molar extinction coefficients and fluorescence quantum yields. Compounds **2**, **5**, and **6** showed their strongest emission at pH values below the physiologically relevant range, consistent with their experimentally determined pK_a values derived from pH-dependent fluorescence measurements (Table 2). Conversely, compounds **1** and **7** retained significant fluorescence at pH 7.4 and, combined with their excellent aqueous solubility, represent promising starting points for further probe development.

Compound **8** is particularly notable as the only derivative that emits in the red region of the spectrum. Red-emitting fluorophores are highly advantageous for biological applications due to reduced cellular autofluorescence [13]. In addition, compound **8** exhibits a pK_a of 5.0 and displays minimal fluorescence at pH 7.4, while showing strong emission under acidic conditions comparable to those found in the lysosomal lumen (pH 4.5–5.0). Accordingly, compound **8** was selected for further evaluation as a potential live-cell lysosome probe.

Given that structurally related fluorophores such as **IMQU-8** or **IPQC** have previously been used as lysosome labels, and that compound **1** displays a similar pH-dependent fluorescence profile, compound **1** was also included in subsequent lysosomal labelling studies, despite exhibiting significant quantum yield at pH 7.4.

3.3. Microscopy

To test the performance of **1** and **8** as lysosome labels, they were added to an adherent layer of live lung epithelial cells (LA-4 cell line) together with the commercially available lysosome label Lysotracker

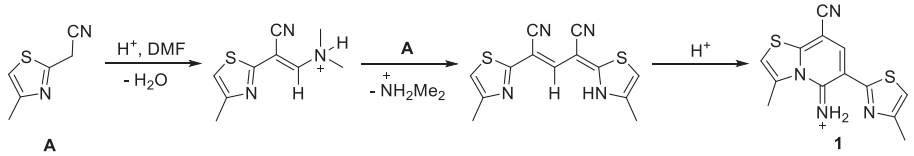

Scheme 3. Proposed mechanism of reaction forming NBFP **1**.

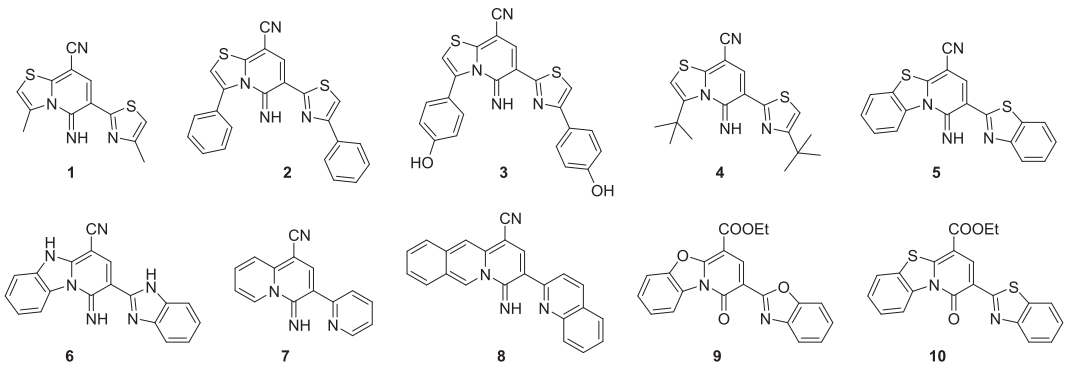

Fig. 1. Structures of all synthesized compounds. Compounds **1**–**8** were isolated in the form of salts corresponding to the acids employed as catalysts in the reaction mixtures.

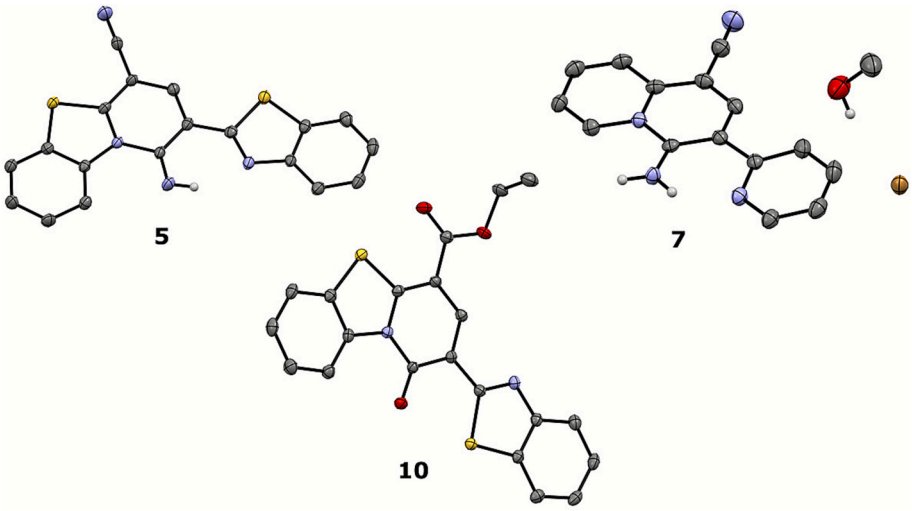

Fig. 2. Crystal structures of compounds **5**, **7**•HBr•MeOH and **10**. Thermal ellipsoids are drawn at 50% probability level and carbon-bound hydrogen atoms are omitted for better clarity.

Red DND-99, and imaged using confocal fluorescence microscopy. Interestingly, although both **1** and **8** quickly labelled vesicles in the cells, their colocalisation with lysosomes was not as expected. **1** only partly colocalized with Lysotracker Red, whereas **8** did not colocalize with it (Fig. 4A, Fig. S10, Fig. S11).

Lysosome-selective labelling by small-molecule probes commonly relies on pH-dependent trapping: a weakly basic amine (e.g., dimethylamino or morpholine group) enables the neutral probe to freely diffuse across membranes, but becomes protonated in the acidic lysosomal lumen, preventing the probe's diffusion back into the cytosol [14,15]. This mechanism, exploited by BODIPY-based LysoTracker Red, could in principle also apply to probes **1** and **8**, which are non-protonated and weakly emissive at neutral pH but become protonated and strongly fluorescent under acidic conditions.

The incomplete colocalization observed for **1** can be attributed to its pH-dependent fluorescence response, which remains significant across both neutral and acidic pH values (Fig. 3 Bottom). Consequently, **1** likely labels not only lysosomes but also other vesicular or slightly acidic compartments. In contrast, although the fluorescence of **8** is prominent only below pH 6 (Fig. 3 Top), its emission appears to originate from non-lysosomal structures. The poor aqueous solubility of **8**, combined with its high lipophilicity (calculated logP = 3.39; ChemDraw 22.2.0.3300, PerkinElmer), may lead to off-target staining [16].

The suitability of compounds **1** and **8** for long-term live-cell imaging was evaluated next. LA-4 cells were incubated with each probe (20 μM) in complete culture medium for three hours under stage-top incubation conditions. During this period, morphological changes in nuclear structure were observed in a subset of cells treated with compound **8** (Fig. S12), whereas no noticeable alterations in cellular or organelle morphology were detected for compound **1**.

Cytotoxicity was subsequently evaluated using a range of probe concentrations, with 40 μM being the highest concentration tested. An MTS assay was employed for compound **1**, while a resazurin-based PrestoBlue assay was used for compound **8** due to spectral interference with the MTS assay. Neither compound showed significant cytotoxicity after 24 h incubation at any of the tested concentrations. These results are consistent with the microscopy observations for compound **1**. In contrast, the absence of reduced metabolic activity in the viability assay for compound **8** suggests that the observed morphological changes may not arise from acute cytotoxicity but could instead reflect phototoxic effects, such as the generation of reactive oxygen species upon illumination. Further investigation of this phenomenon is warranted but lies beyond the scope of the present study.

Another advantage of **1** for long-term imaging is its low signal of unbound dye in the medium (Fig. S13). Thus, long-term imaging could be performed without washing the unbound dye, which reduces the bleaching effect by allowing the continuous exchange of the bleached dye in cellular structures with the large amount of non-bleached dye in the medium [17]. The background signal of **8** was noticeable, but still lower than the signal from the cell structures (Fig. S13).

Next, we tested the compatibility of both compounds with high-resolution Stimulated Emission Depletion (STED) microscopy.

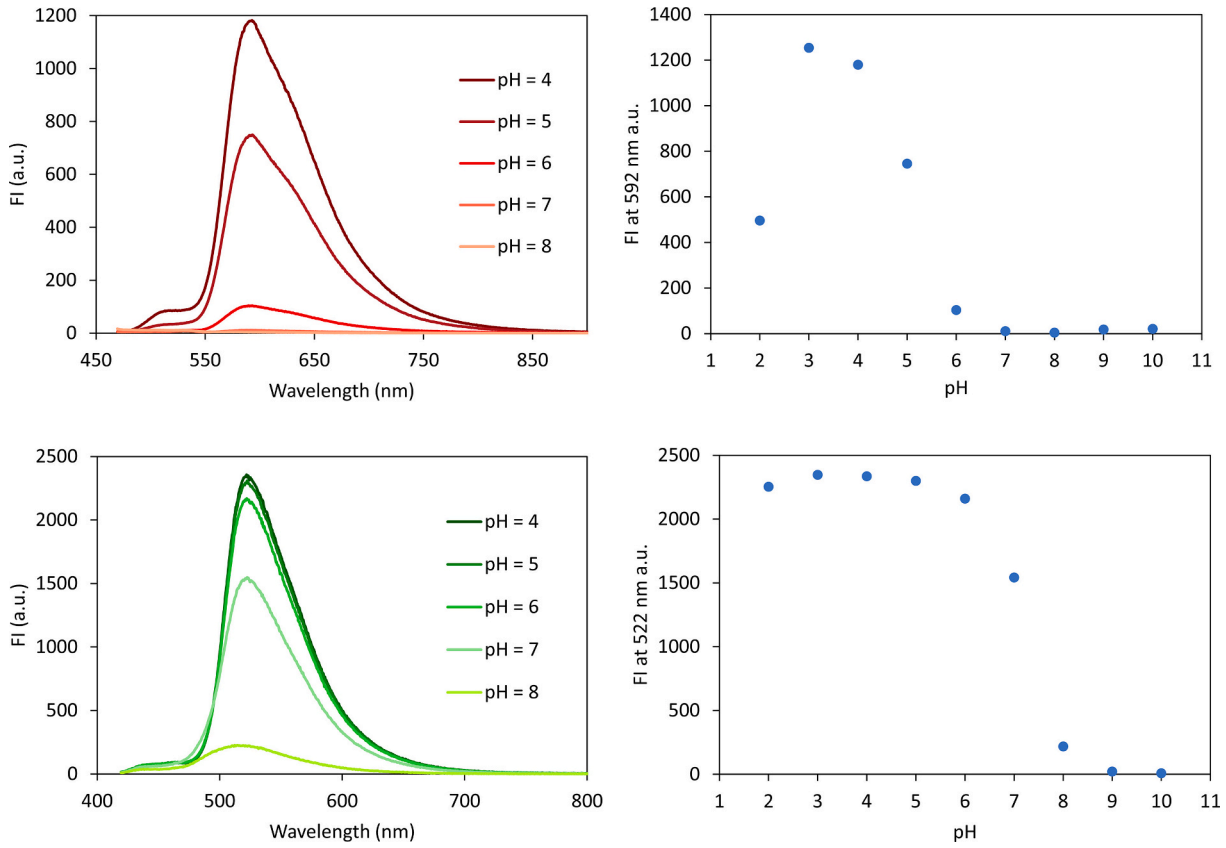

Fig. 3. Top left: Emission spectra of **8** (1 μM) in buffers ranging from pH 4 to 8. Top right: Fluorescence intensity at 592 nm of **8** as a function of pH. Bottom left: Emission spectra of **1** (1 μM) in buffers ranging from pH 4 to 8. Bottom right: Fluorescence intensity at 522 nm of **1** as a function of pH. For a comprehensive view of the spectra across the full pH range (pH 2–10) for compounds **2**–**7**, refer to Fig. S6 in the Supplementary data. FI – fluorescence intensity.

Table 2
Photophysical properties of compounds **1**, **2**, and **5**–**8** were measured in Britton–Robinson universal buffer at pH 3.0. Absorption maxima (λ_{abs}), emission maxima (λ_{em}), and molar extinction coefficients (ε) were determined at pH 3.0, while fluorescence quantum yields (Φ) were measured at pH 3.0 and pH 7.4. Apparent pK_a values were obtained by fitting the pH-dependent fluorescence intensity over the pH range 2–10. Photophysical properties of compounds **9** and **10** were determined in absolute ethanol. Details of the experimental procedures and data analysis are provided in the Supplementary data.

Compound	λ_{abs} (nm)	λ_{em} (nm)	ε (cm^{-1} M^{-1})	Φ	pK_a
1	404	522	12,100	0.34/0.31	7.2
2	409	523	9200	0.07/0.02	3.5
5	428	539	8200	0.46/0.04	4.1
6	397	453	15,300	0.30/0.13	3.8
7	392	527	10,500	0.33/0.26	7.6
8	461	589	22,000	0.14/0.01	5.0
9	372	423	30,500	0.84	/
10	427	437	18,000	0.96	/

However, neither of the probes showed an improvement of resolution in STED microscopy when using a 775 nm STED laser (Fig. S14). This is likely the consequence of their low emission at the STED laser wavelength as seen on Fig. 3. Both probes also bleached significantly during continuous STED imaging with high laser powers – even without washing the unbound probe. In confocal imaging however, **1** was effectively more photostable than **8** (Fig. S15).

Importantly, we observed that both **1** and **8** are spectrally sensitive, i.e. the spectral properties of the probes change according to the probe's environment. As shown on Fig. 4B and Fig. S16, the distribution of the fluorescence signal in images of labelled cells changed when different excitation lasers and detection windows were used to image the same part of the sample. We also observed that both **1** and **8** had different fluorescence lifetimes (FLIM) in different labelled organelles, with the lifetime changes of **1** being larger than those of **8** (Fig. 4C, Fig. S12). We also observed that **1** has a longer overall lifetime than **8**, which in general implies that **1** has a smaller number of available non-radiative decay pathways, resulting in a higher quantum yield.

To assess the environmental sensitivity of compounds **1** and **8**, their fluorescence lifetime was measured in solvents of various polarities, viscosities and pH (compound concentration 10 μM). The fluorescence lifetime of compound **8** decreased both due to increased viscosity and increased pH, complicating the interpretation of the lifetime measurements in cells. We also noticed that it exhibited a larger fluorescence signal in less polar solvents. On the other hand, the lifetime of compound **1** was strongly influenced by the polarity of the solvent (6 ns in non-polar solvents and 1.5 ns in polar solvents), but was not influenced by changes in viscosity or pH. Thus, this compound could be used to sense intra-cellular polarity. Namely, a unique advantage of ratiometric and fluorescence lifetime imaging for sensing the physicochemical properties of the intracellular environment is that the readout is independent from the dye concentration and the experimental setup – in contrast to intensity-based measurements [18,19]. We also observed an increase in fluorescence signal with decreased solvent polarity, leading us to assume that the vesicles that are labelled with compound **1** but not Lysotracker Red (Fig. 4), could be non-polar lipid droplets.

4. Conclusion

In this study, we developed a simple and efficient synthetic route to access structurally diverse nitrogen bridgehead fused pyridines (NBFPs) from readily available arylacetonitriles and DMF under acidic conditions. The reaction mechanism was investigated using a deuterated

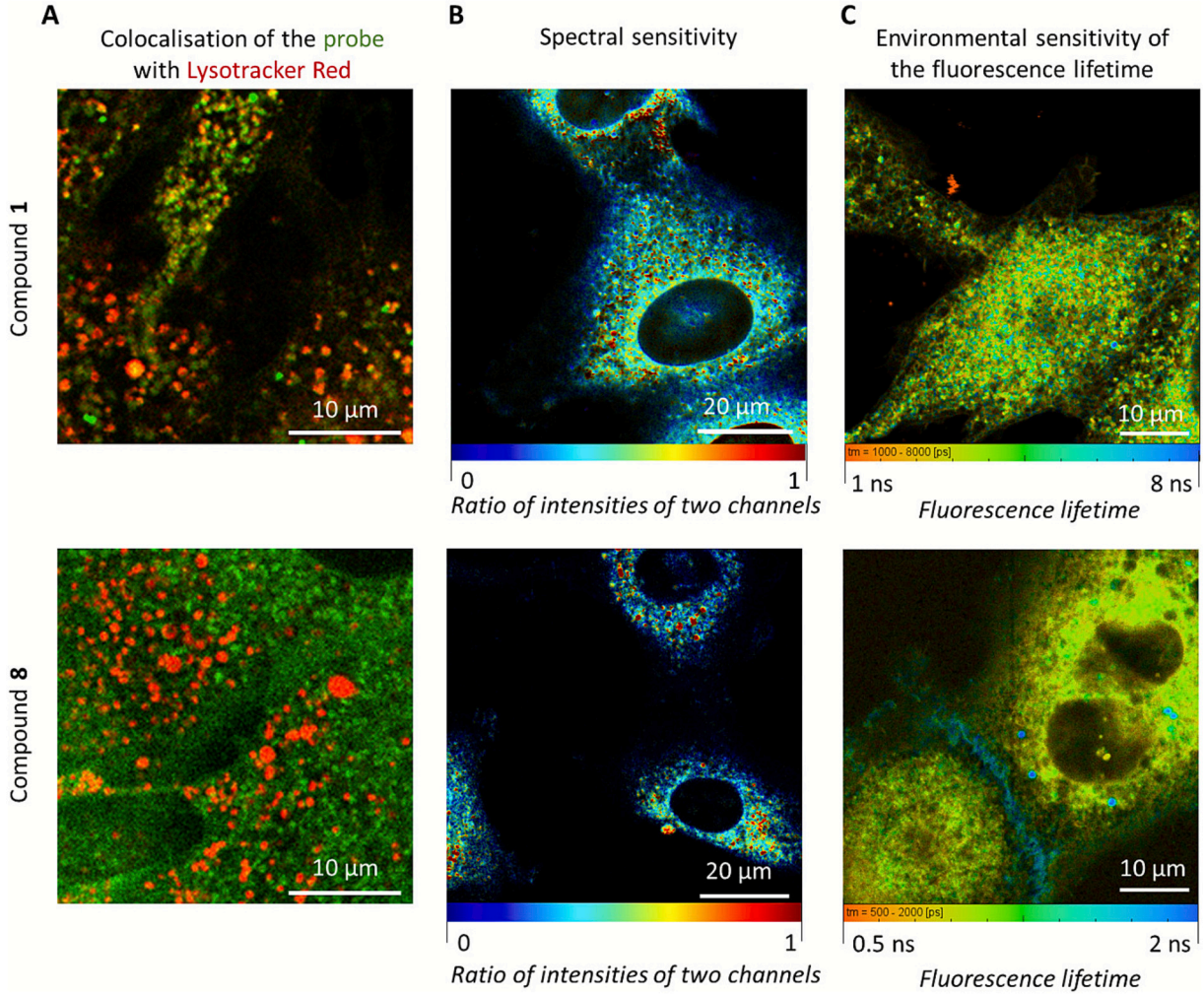

Fig. 4. A: Colocalization of **1** (green, top) and **8** (green, bottom) with Lysotracker Red (red). B: Spectral sensitivity of **1** and **8**, demonstrated as the ratio between an image, obtained with excitation/emission 405 nm/651–720 nm, and an image, obtained using the combination 488 nm/581–627 nm. C: Fluorescence lifetime (FLIM) images of **1** and **8**. The brightness of images in B and C is increased to better emphasize the difference in ratios and lifetimes. (For interpretation of the references to colour in this figure legend, the reader is referred to the web version of this article.)

reagent and LCMS analysis of the reaction mixtures, and the influence of various acid catalysts on reaction yield was systematically evaluated. The obtained fluorophores exhibited pH-sensitive emission, with several compounds showing large Stokes shifts, highlighting their potential as bioimaging probes. Among the synthesized derivatives, compounds **1** and **8** were further assessed in live-cell imaging experiments. Although they showed only partial or no colocalization with the lysosomal marker LysoTracker Red, both compounds demonstrated environment-dependent fluorescence suitable for ratiometric and fluorescence-lifetime-based intracellular sensing. Compound **1** proved particularly promising, combining low background fluorescence, localization in both acidic and neutral vesicles, negligible cytotoxicity and environmental sensitivity to the polarity of its surroundings. These findings warrant further optimization of this probe, focusing on improving photostability, conducting a comprehensive cytotoxicity assessment, and achieving a deeper characterization of its environmental sensitivity to advance its potential in live-cell imaging applications.

CRediT authorship contribution statement

Hana Kokot: Writing – review & editing, Writing – original draft, Visualization, Methodology, Investigation, Formal analysis. **Aljoša Bolje:** Writing – review & editing, Methodology, Investigation, Formal analysis. **Jakob Kljun:** Writing – review & editing, Visualization, Investigation, Funding acquisition, Formal analysis. **Andraž Bevk:** Investigation. **Natalija Trunkelj:** Formal analysis, Investigation, Methodology. **Lucija Peterlin Mašič:** Formal analysis, Funding acquisition, Methodology. **Janez Mravljak:** Writing – original draft, Visualization, Supervision, Project administration, Investigation, Funding acquisition, Conceptualization. **Stane Pajk:** Writing – original draft, Visualization, Supervision, Project administration, Investigation, Funding acquisition, Conceptualization.

Declaration of competing interest

The authors declare the following financial interests/personal relationships which may be considered as potential competing interests: Stane Pajk reports financial support was provided by Slovenian Research and Innovation Agency. If there are other authors, they declare that they have no known competing financial interests or personal relationships that could have appeared to influence the work reported in this paper.

Acknowledgments

This work was supported by the Slovenian Research and Innovation Agency (core research funding P1-0208, P1-0060 and P1-0175 and project J3-3079), European Regional Development Fund OP20.05187 RI-SI-EATRIS. The authors acknowledge financial support from the

Ministry of Education, Science, and Sport, Republic of Slovenia (Grant 5442-1/2018/405). The authors also acknowledge the support of the Centre for Research Infrastructure at the University of Ljubljana, Faculty of Chemistry and Chemical Technology, which is part of the Network of Research and Infrastructural Centres UL (MRIC UL) and is financially supported by the Slovenian Research and Innovation Agency (Infrastructure programme No. I0-0022) for the use of the Supernova diffractometer.

Appendix A. Supplementary data

Supplementary data to this article can be found online at https://doi.org/10.1016/j.jphotochem.2026.117068.

Data availability

Data will be made available on request.

References

[1] J. Ma, R. Sun, K. Xia, Q. Xia, Y. Liu, X. Zhang, Design and application of fluorescent probes to detect cellular physical microenvironments, Chem. Rev. 124 (2024) 1738–1861, https://doi.org/10.1021/acs.chemrev.3c00573.

[2] X. Wang, Q. Ding, R.R. Groleau, L. Wu, Y. Mao, F. Che, O. Kotova, E.M. Scanlan, S. E. Lewis, P. Li, B. Tang, T.D. James, T. Gunnlaugsson, Fluorescent probes for disease diagnosis, Chem. Rev. 124 (2024) 7106–7164, https://doi.org/10.1021/acs.chemrev.3c00776.

[3] G. Jiang, H. Liu, H. Liu, G. Ke, T. Ren, B. Xiong, X. Zhang, L. Yuan, Chemical approaches to optimize the properties of organic fluorophores for imaging and sensing, Angew. Chem. Int. Ed. 63 (2024) e202315217, https://doi.org/10.1002/anie.202315217.

[4] W. Song, L. Xiong, X. Li, Y. Zhang, B. Wang, G. Liu, W. Li, Y. Yang, Y. Tang, Fluorpredictor: an interpretable tool for multiproperty prediction and retrieval of fluorescent dyes, J. Chem. Inf. Model. 65 (2025) 2854–2867, https://doi.org/10.1021/acs.jcim.5c00127.

[5] Y. Kim, S. Kang, B.H. Lee, Y. Song, S. Kang, H.Y. Park, Y. Lee, De novo generation of a bright blue fluorophore from 2-oxoglutarate in biological samples, Chem. Sci. 13 (2022) 365–372, https://doi.org/10.1039/D1SC05808H.

[6] L. Zhang, C. Wang, Y. Jiang, H. Li, H. Wang, H. Long, P. Liu, X. Xu, T. Yang, Selective and sensitive detection and detoxification of Pd2+ in living cells with a water-soluble fluorescent probe, Anal. Chim. Acta 1204 (2022) 339728, https://doi.org/10.1016/j.aca.2022.339728.

[7] T. Yang, H. Li, Z. Cao, Y. Yang, D. Zheng, P. Liu, C. Peng, H.F. Schaefer, Y. Luo, Ultrafast and reversibly cyclization/cycloreversion of 4-imino-4H-Quinolizine-1-Carbonitrile: a new strategy for fluorescence modulation in pH sensing in living cells, Dyes Pigments 195 (2021) 109694, https://doi.org/10.1016/j.dyepig.2021.109694.

[8] Y.-P. Gong, J. Yang, J.-W. Fang, Q. Li, Z.-Y. Yu, A. Guan, H.-Y. Gong, A DNA small molecular probe with increasing K^+ concentration promoted selectivity, RSC Adv. 11 (2021) 15030–15035, https://doi.org/10.1039/D0RA06274J.

[9] D.S. Milokhov, O.V. Khilya, A.V. Turov, V.V. Medviediev, O.V. Shishkin, Y. M. Volovenko, Hydroxypropyl substituted nitrogen bridgehead fused cyanopyridines, Tetrahedron 70 (2014) 1214–1222, https://doi.org/10.1016/j.tet.2013.12.074.

[10] O.V. Dolomanov, L.J. Bourhis, R.J. Gildea, J.A.K. Howard, H. Puschmann, ıt OLEX2: a complete structure solution, refinement and analysis program, J. Appl. Crystallogr. 42 (2009) 339–341, https://doi.org/10.1107/S0021889808042726.

[11] C.F. Macrae, P.R. Edgington, P. McCabe, E. Pidcock, G.P. Shields, R. Taylor, M. Towler, J. van de Streek, ıt mercury: visualization and analysis of crystal structures, J. Appl. Crystallogr. 39 (2006) 453–457, https://doi.org/10.1107/S002188980600731X.

[12] X. Subirats, E. Fuguet, M. Rosés, E. Bosch, C. Ràfols, Methods for pKa determination (I): Potentiometry, spectrophotometry, and capillary electrophoresis, in: Reference Module in Chemistry, Molecular Sciences and Chemical Engineering, Elsevier, 2015, https://doi.org/10.1016/B978-0-12-409547-2.11559-8. B9780124095472115598.

[13] M. Dai, Y.J. Yang, S. Sarkar, K.H. Ahn, Strategies to convert organic fluorophores into red/near-infrared emitting analogues and their utilization in bioimaging probes, Chem. Soc. Rev. 52 (2023) 6344–6358, https://doi.org/10.1039/D3CS00475A.

[14] W.-W. Xiao, S. Chen, M.-X. Liu, Y.-L. Yu, Fluorescent probes for lysosomes, mitochondria, and lipid droplets: precision design, dynamic microenvironment monitoring, and heterogeneity exploration, Chem. Commun. 61 (2025) 7929–7944, https://doi.org/10.1039/D5CC01767J.

[15] X. Duan, Q. Tong, C. Fu, L. Chen, Lysosome-targeted fluorescent probes: design mechanism and biological applications, Bioorg. Chem. 140 (2023) 106832, https://doi.org/10.1016/j.bioorg.2023.106832.

[16] S.H. Alamudi, R. Satapathy, J. Kim, D. Su, H. Ren, R. Das, L. Hu, E. Alvarado-Martínez, J.Y. Lee, C. Hoppmann, E. Peña-Cabrera, H.-H. Ha, H.-S. Park, L. Wang, Y.-T. Chang, Development of background-free tame fluorescent probes for intracellular live cell imaging, Nat. Commun. 7 (2016) 11964, https://doi.org/10.1038/ncomms11964.

[17] C. Spahn, J.B. Grimm, L.D. Lavis, M. Lampe, M. Heilemann, Whole-cell, 3D, and multicolor STED imaging with exchangeable fluorophores, Nano Lett. 19 (2019) 500–505, https://doi.org/10.1021/acs.nanolett.8b04385.

[18] M. Schäferling, Nanoparticle-based luminescent probes for intracellular sensing and imaging of pH, WIREs Nanomed. Nanobiotechnol. 8 (2016) 378–413, https://doi.org/10.1002/wnan.1366.

[19] R. Datta, T.M. Heaster, J.T. Sharick, A.A. Gillette, M.C. Skala, Fluorescence lifetime imaging microscopy: fundamentals and advances in instrumentation, analysis, and applications, J. Biomed. Opt. 25 (2020) 1, https://doi.org/10.1117/1.JBO.25.7.071203.